

A Flexible and Modular Receiver Coil Array for Magnetic Resonance Imaging

Jhy-Neng Tasso Yeh^{ID}, Student Member, IEEE, Jo-Fu Lotus Lin, Yi-Tien Li, and Fa-Hsuan Lin^{ID}, Member, IEEE

Abstract— We propose a flexible form-fitting MRI receiver coil array assembled by individual coil modules. This design targets MRI applications requiring a receiver array conforming to the anatomy of various shapes or sizes. Coil modules in our proposed array were arranged with gaps between them. Each coil module had a circumferential shielding structure stacked on top of the coil. Together they achieve robust decoupling when the array was bent differently. Two types of the circumferential shielding structure were investigated by using full-wave electromagnetic simulations and imaging experiments. Results showed that our flexible coil array had good decoupling between coils whether they were on a flat or curved surface with the S_{21} magnitude ranged between -18.1 dB and -19.9 dB in simulations, and with the average of off-diagonal entries of the noise correlation matrix less than 0.047 in experimental measurements. Anatomical images of human brain, calf, and knee were acquired by our seven-channel prototype on a 3T MRI system. The maximal and the average SNR within 50 mm from our array surpassed those from the commercial 32-channel head and 4-channel flexible coil arrays by 2.63/1.35-fold and 3.89/1.50-fold, respectively.

Index Terms— Circumferential shielding, coil array, flexible, magnetic resonance imaging (MRI), modular, mutual coupling.

I. INTRODUCTION

MAGNETIC resonance imaging (MRI) receiver coil arrays can achieve large field-of-view (FOV) and high signal-to-noise ratio (SNR) simultaneously [1]. Combined with parallel imaging techniques [2], [3], a receiver coil array with uncorrelated channel spatial sensitivity enables the accelerated image acquisition with acceptable SNR loss [4]. As the image

Manuscript received May 24, 2018; revised August 17, 2018; accepted August 28, 2018. Date of publication October 2, 2018; date of current version March 1, 2019. This work was supported in part by the Ministry of Science and Technology, Taiwan, under Grant MOST 104-2314-B-002-238 and Grant MOST 103-2628-B-002-002-MY3, in part by the National Health Research Institute, Taiwan, under Grant NHRI-EX107-10727EI, and in part by the Academy of Finland under Grant 298131. (Corresponding author: Fa-Hsuan Lin.)

J.-N. T. Yeh, J.-F. L. Lin, and Y.-T. Li are with the Institute of Biomedical Engineering, National Taiwan University, Taipei 10617, Taiwan.

F.-H. Lin is with the Institute of Biomedical Engineering, National Taiwan University, Taipei 10617, Taiwan, and also with the Department of Neuroscience and Biomedical Engineering, Aalto University, 02150 Espoo, Finland (e-mail: fhlin@ntu.edu.tw).

Color versions of one or more of the figures in this paper are available online at <http://ieeexplore.ieee.org>.

Digital Object Identifier 10.1109/TMI.2018.2873317

SNR acts as an important index for the coil performance, researchers pursue the optimal design of receiver coil arrays to achieve optimal SNR. Since the targeted anatomy can vary significantly in shape and size, the spatial distance between coils and the imaging object affects the signal sensitivity which leads to the resulted image SNR [5]. Seeking a geometry of the coil array for diverse anatomical targets with minimal mutual coupling between coils and optimal performance is a daunting engineering task.

One approach to optimize the image SNR is to tailor the receiver coil array such that it tightly fits to the imaging object. A flexible coil array allows its receiver coils fitting the surface of the imaging object in order to improve the filling factor, which in turn has higher SNR [6]–[12]. A major technical challenge in constructing a flexible coil array is that the mutual coupling between coils is inevitably changed when the coil array is bent differently to fit the object's surface. Conventionally, the surface circular coils in a receiver coil array are decoupled by overlapping adjacent coils. However, adjusting coil overlapping to minimize the decoupling is laborious, and the unique coil positions for the optimal performance prevent the mechanical flexibility of the coil array. Decoupling can also be achieved by inserting inductors and/or capacitors between neighboring coils [13]–[16]. But the soldering on these components introduces extra ohmic loss and also reduces the mechanical flexibility of the coil array. Alternatively, inserting a gap between adjacent coils can achieve decoupling and improve the quality in parallel imaging [17], [18]. Nevertheless, a small gap cannot provide sufficient coil isolation, whereas a large gap may lead to signal void between coils. In addition, when developing a flexible receiver coil array, a modular coil design is desired such that a flexible coil array can be easily assembled. However, the coil decoupling techniques mentioned above cannot offer the sufficient isolation between coils for diverse anatomical shapes and sizes.

Here we propose a flexible coil array design useful for imaging different human anatomy. Specifically, the array consists of coil modules, each of which has a circumferential shielding structure stacked above a circular coil. These coil modules were separated by gaps. First, the gap between coil modules allowed us to bend the coil array in order to tightly fit the imaging object. Second, the stacked circumferential shielding structure provided stable decoupling when

the coil array was bent differently. The shape and size of the circumferential shielding structure were carefully evaluated to obtain the minimal mutual coupling between coil modules and the maximal image SNR, while the gap between coil modules was demanded to be minimized. Different from the coplanar approach [19], our coil had a three-dimensional architecture. The vertically stacked shielding structure allows for a smaller gap between coils to create a more compact coil arrangement. Also, the minimized gap between coil avoided the significant signal void between neighboring coils. With the cost of reduced quality factor (Q) and image SNR for each coil module, the whole flexible coil array can tightly fit to the imaging object and consequently achieve a higher filling factor and sensitivity than a rigid coil array. Compared to previous works [20]–[28], to our knowledge, this work represents the first modular flexible surface coil array utilizing a stacked circumferential shielding structure allowing for high filling factor and high SNR at different bending conditions. Here we specifically investigated two types of circumferential shielding structures and compared their performances by full-wave electromagnetic simulations and MR imaging experiments. A prototype of seven-channel flexible receiver coil array was constructed and tested on a 3T MRI system to image both a phantom and a human participant. For comparison, images of the same participant were also acquired with commercial coil arrays. In Section II, we present the details of full-wave electromagnetic simulations, the construction of coil modules, bench measurements, and *in vivo* imaging experiments. In Section III, we show results of electromagnetic simulations and imaging experiments. In Section IV, we concluded this study by discussing results and future studies based on the current coil array prototype.

II. METHODS

A. Full-Wave Electromagnetic Modeling

The full-wave electromagnetic simulations were conducted with HFSS (ANSYS, Canonsburg, USA) and the setup is illustrated in Fig. 1(a) to Fig. 1(c) [10], [11]. A dual-loop probe consisting of two decoupled loops made by perfect electrical conductor (PEC) was located above the center of circular coil in the positive X-axis. This PEC dual-loop probe generated circularly-polarized component of the B_1 magnetic field to numerically excite spins in the phantom [29] and measured the scattering parameter S_{21} of dual-loop probe itself to evaluate the isolation between coil modules. In this work, the direction of excitation signal of PEC dual-loop probe was defined such that the component \vec{B}_1^+ tipping down the magnetization. The circularly-polarized magnetic fields of the coil array at the axial plane through the center of cylindrical phantom (*i.e.*, the XY plane in Fig. 1) was calculated [30]:

$$\begin{aligned}\vec{B}_1^+ &\equiv \frac{1}{2} \left(\vec{B}_x + j \vec{B}_y \right) \\ &= \frac{1}{2} \left\{ \left[re(\vec{B}_x) - im(\vec{B}_y) \right] + j \left[im(\vec{B}_x) + re(\vec{B}_y) \right] \right\}\end{aligned}\quad (1a)$$

and

$$\begin{aligned}\vec{B}_1^- &\equiv \frac{1}{2} \left(\vec{B}_x - j \vec{B}_y \right)^* \\ &= \frac{1}{2} \left\{ \left[re(\vec{B}_x) + im(\vec{B}_y) \right] - j \left[im(\vec{B}_x) - re(\vec{B}_y) \right] \right\},\end{aligned}\quad (1b)$$

where subscripts x and y indicate the orientation of the directional component of the magnetic field, $j = \sqrt{-1}$, the asterisk indicates the complex conjugate, and $re()$ and $im()$ are the real and imaginary component of the argument, respectively. The excitation signal was defined as a frequency-sweep continuous wave, which was between 115 MHz and 135 MHz in steps of 0.125 MHz with 1 watt of power, generated from a virtual source with $50\ \Omega$ internal impedance. To calibrate the strength of excitation signals, the electromagnetic fields were normalized such that a rectangular excitation pulse of 3 ms duration excited 90° flip angle at the center of circular coil in the positive X-axis [30]. Thus, the calibration factor of excitation signal power, W_n , was determined as

$$W_n \equiv \left(\frac{\alpha}{\gamma \tau |\vec{B}_1^+|} \right)^2 = \left(\frac{2\pi \cdot \frac{90}{360}}{\gamma \tau |\vec{B}_1^+|} \right)^2 \cong \left(\frac{1.9571}{|\vec{B}_1^+|} \right)^2 \quad (2)$$

where γ is the gyromagnetic ratio of proton ^1H , and τ is the duration of rectangular excitation pulse.

The receiver coil array consisted of two circular coils, each of which had 50 mm diameter and 5 mm coil width, modeled by a copper sheet (0.02 mm thickness, $\epsilon_r = 1$, $\sigma = 58 \times 10^6\ \text{S/m}$) coating on a FR4 substrate (0.6 mm thickness, $\epsilon_r = 4.4$, $\tan\delta = 0.02$). Two types of circumferential shielding structures stacked above the circular coil were modeled. Suggested by previous works [23], [25], the first shielding structure had a single strip (shielding type SA, Fig. 1(a)). In order to investigate the influence of different geometries of shielding structure on decoupling degrees and resulted SNRs, the second shielding structure consisted of two parallel strips (shielding type SB, Fig. 1(b)). The positions and dimensions of both circumferential shielding structures were iteratively adjusted to maximize the isolation between adjacent coil modules (shielding type SA: 50 mm diameter, 1 mm distance to circular coil perimeter, 3 mm strip width; shielding type SB: 50 mm diameter, 1 mm distance to circular coil perimeter, 1 mm strip width, 3 mm total spatial height with 1 mm interior gap in between two parallel strips). A two-channel coil array without either shielding structure was used as the control array in order to compare the performance due to the shielding structure. All adjacent circular coils had a fixed 2 mm gap between them regardless of without or with a shielding structure. Three evenly distributed capacitors of the same geometrical size and capacitance value were inserted at the circular coil for tuning at the desired resonance frequency (exact 125 MHz). A liquid-filled cylindrical phantom (200 mm diameter, 200 mm length, 5 mm shell thickness; shell material $\epsilon_r = 4.6$, $\sigma = 0\ \text{S/m}$, core material $\epsilon_r = 42.9$, $\sigma = 0.9\ \text{S/m}$) was placed beneath the two-channel coil array to simulate the loading of a human body.

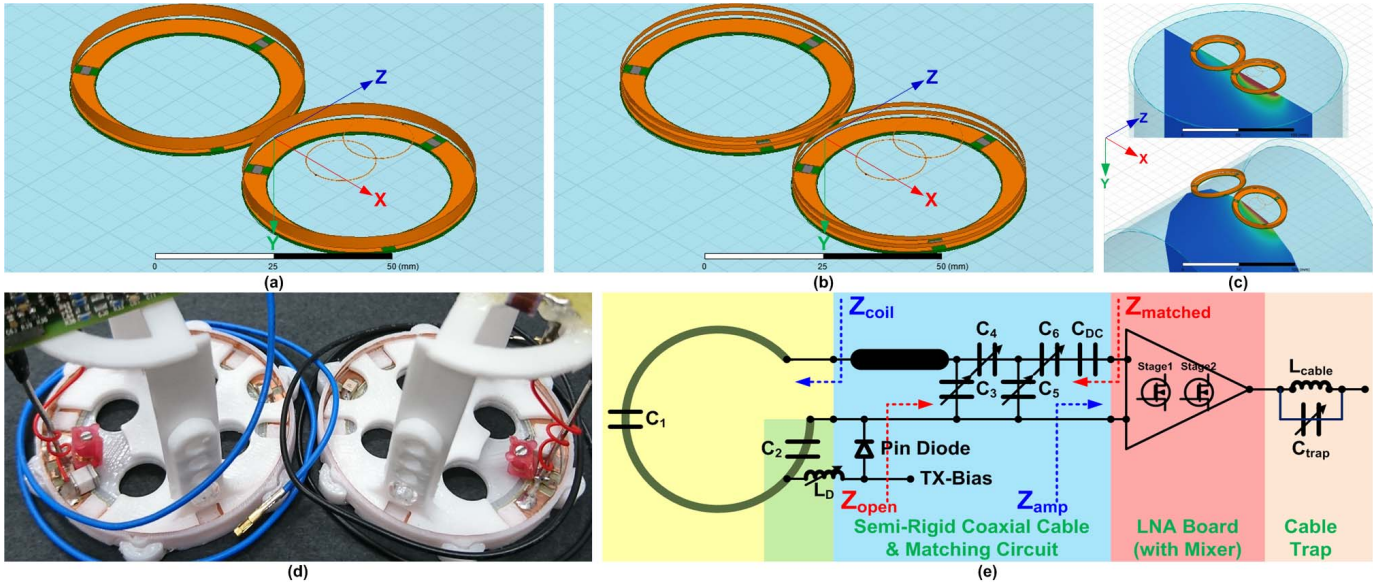


Fig. 1. Simulation setup for a two-channel coil array equipped with either (a) type SA or (b) type SB circumferential shielding structure. The PEC dual-loop probe located above the center of one circular coil generated the excitation signal and measured the scattering parameter S_{21} . (c) The cylindrical phantom (in light-blue) provided a flat or curved surface. (d) Illustrations of modular coils of shielding type SA (left) and type SB (right). (e) Schematic diagram of the detuning circuit, matching circuit, and cable trap.

To investigate the flexibility of the coil array, we changed the relative position of two coil modules and evaluated the degree of isolation between them. Specifically, the two-channel coil array was first placed on the flat surface of cylindrical phantom (Fig. 1(c) top) and the capacitors on the coils were adjusted to tune both coil modules in resonance. Then the same coil array was bent such that the normal directions of the two coils matched the radial direction of the cylindrical phantom without changing the capacitance values (Fig. 1(c) bottom). Each coil module including the coil conductor and the coil substrate was rigid and cannot be bent.

B. Design of Coil Module

To investigate the performance of isolation degree between adjacent coil modules, we constructed two two-channel coil arrays equipped with circumferential shielding type SA and type SB described in the previous section. A two-channel coil array without either shielding structure was also constructed for performance comparison. Two modular coils were shown in Fig. 1(d). The circular coil loops (50 mm diameter, 5 mm coil width) were built from a FR4 printed circuit board (0.6 mm thickness, 18 μ m single copper layer, Nan-Ya PCB Co., Taiwan). Coils had evenly distributed capacitors (ATC 100 B series, American Technical Ceramics, NY, USA). The circumferential shielding structure was built from a copper foil strip (3 mm and 1 mm width for shielding type SA and type SB, respectively). The assembly of circular coil and the stacked shielding structure was connected to a low-noise preamplifier (LNA) integrated with a mixer (Siemens, Erlangen, Germany) through a semi-rigid coaxial cable (50 mm length, SUKOFORM_47 CU, Huber+Suhner AG., Switzerland) and a custom-made matching circuit shown in Fig. 1(e). The matching circuit had a balanced circuit design with 4 trimmer-capacitors ($C_3 - C_6$, JR400, Voltronics, NJ, USA), transformed

the impedance at the input terminal of LNA to 50Ω in order to achieve the lowest noise figure (less than 0.6 dB). An active detuning circuit composed using a PIN diode (M/A-COM Tech., MA, USA) in series with a tunable inductor (Coilcraft, IL, USA). During the transmission phase, the PIN diode was forward biased to create a resonance circuit (L_D, C_2) and the coil was detuned consequently. The output terminal of LNA was connected to a cable trap to suppress the shield current. This cable trap with a high impedance was constructed by a hand-wound loop in parallel with a trimmer-capacitor.

The mechanical housing of the coil array was manufactured by a 3D-printer (FORTUS 400mc, Eden Prairie, MN, USA) using the bio-compatible materials of poly-carbonate plastic. For each coil module, the mechanical housing consisted of a flat rigid substrate (50 mm diameter, 0.8 mm thickness), a short cylinder (50 mm diameter, 3 mm height for shielding type SA and type SB, or 1 mm height for the control coil), and a LNA supporting shelf (irregular shape, about 45 mm diameter \times 50 mm height). All coil modules were placed with a 2-mm gap between each other on a 0.6-mm thick flexible thermoplastic-elastomer substrate.

C. Bench and Experimental Measurements

First, each coil module in the control coil array and the proposed coil arrays equipped with shielding type SA or type SB was placed on the flat surface of a 200-mm diameter acrylic hemispherical phantom filled with distilled water. The coils were tuned to the Larmor frequency of proton at 3T (123.25 MHz) and simultaneously applied the technique of preamplifier decoupling [1] by adjusting capacitance values of C_3, C_4, C_5 , and C_6 . We conducted two S_{21} measurements using a custom-made dual-loop probe, which had $|S_{21}|$ less than -60 dB as it was away from the coil array, on a vector

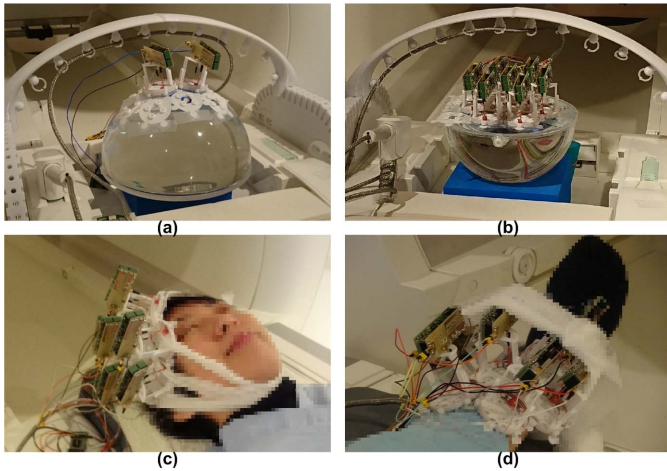


Fig. 2. Experimental setups for (a) two-channel flexible coil array fitted on the curved surface of a phantom of 200 mm diameter, (b) seven-channel flexible coil array horizontally placed on the flat surface of a phantom of 200 mm diameter, (c) seven-channel flexible coil array placed on the right temporal site of a participant's head, and (d) seven-channel flexible coil array wrapped around the participant's calf. The same setups were applied for imaging the participant's knee.

network analyzer (ZVL3, Rohde-Schwarz, Germany). In two measurements, a 50Ω terminator and a preamplifier was respectively attached to the coil matching circuit when the coil was tuned (PIN diode was reverse biased). The peak of $|S_{21}|$ curve in the first measurement and the ‘dip’ in the second measurement were at the Larmor frequency after adjusting trimmer-capacitors. The capacitance values were kept unchanged in all subsequent imaging experiments. The mutual coupling between coil modules was quantified by measuring the S_{21} of the dual-loop probe. The required detuning setting during the transmission phase was also obtained by measuring the dual-loop probe S_{21} with the forward biased PIN diode. The unloaded Q value of the coil were measured by the dual-loop probe without a terminator attached to the matching circuit. The loaded Q value was similarly measured when the coil was placed close to a human head.

Fig. 2 illustrates the setups of the imaging experiments on a 3T MRI system (Magnetom Skyra, Siemens, Erlangen, Germany). Our custom-made coil arrays only served as the receiver while the body coil of the MRI excited the MRI signal. The coil arrays were mounted on three acrylic hemispherical phantoms of different sizes (150 mm, 200 mm, and 250 mm diameter) filled with distilled water separately in order to test the performance at different curvatures. Our flexible coil arrays were either placed on the flat surface or bent to conform to the curved surface of the hemispherical phantom. The isolation between neighboring coil channels was quantified by a noise correlation matrix, which was calculated from the imaging data without any radio-frequency excitation using an echo-planner imaging pulse sequence (FOV = 256 mm × 256 mm, slice thickness = 256 mm, TR = 100 ms, TE = 30 ms, flip angle = 0°, BW = 2520 Hz/pixel). SNR maps were measured using a gradient-echo pulse sequence (FOV = 178 mm × 178 mm, slice thickness = 5 mm, TR = 462 ms, TE = 10 ms, flip angle = 25°, BW =

260 Hz/pixel). The experimental images were combined between coil modules using the root-sum-of-squares (RSS) reconstruction [1]:

$$SNR_{RSS} = \sqrt{(S^T \Psi^{-1} S^*)}, \quad (3)$$

where S is the column vector containing the complex signals from individual coils, Ψ is the noise covariance matrix, the superscript T denotes the transpose, and the asterisk indicates the complex conjugate.

A seven-channel coil array equipped with shielding type SB was constructed for human imaging. One healthy volunteer participated in our imaging experiments. The participant gave written consent and the study was approved by the Institutional Review Board of National Taiwan University Hospital. To compare with our flexible coil array, we also used two commercial coil arrays to acquire control images. They were a 32-channel head coil array (Siemens, Erlangen, Germany) for human brain imaging and a 4-channel flexible coil array (FlexSmall, Siemens, Erlangen, Germany) for human calf and knee imaging. While the coil size and channel number of these two commercial arrays were different from our flexible coil arrays, these two arrays were the best available choice for comparison in a clinical environment. The diameter sizes estimated from resulted images among all coils of the 32-channel head coil array were about 75 mm to 90 mm. The size of a single coil of the 4-channel flexible coil array was about 160 mm × 80 mm. The distance between the rigid head coil and the subject in the imaging experiment was about 15 mm to 20 mm. Notice that different coil diameters affect the SNR distribution in different depth from the coil surface. High resolution anatomical images were measured using a MPRAGE pulse sequence (FOV = 256 mm × 256 mm, slice thickness = 1 mm, TR = 2530 ms, TE = 3.34 ms, flip angle = 7°, BW = 200 Hz/pixel).

III. RESULTS

A. Numerical Simulations

Fig. 3(a) shows the simulation results of S_{21} magnitude curves of the PEC dual-loop probe when two control coils without either shielding structure were placed on the flat surface of a cylindrical phantom with different gap distances. The curves with a gap less than 22 mm had evident split peaks around 125 MHz. With a gap larger than 26 mm the curves presented a single peak. Fig. 3(b) and Fig. 3(c) show the simulations of S_{21} magnitudes of the PEC dual-loop probe when a two-channel coil array equipped with either shielding type SA or type SB was placed on the flat surface or bent to fit the curved surface of a cylindrical phantom. In both flat and bending conditions, the coil arrays with shielding type SA or type SB had a single peak at 125 MHz. This was distinctly different from the split peaks from control coils. Notice that all two-channel arrays were placed with the same 2 mm gap between coils. These simulations demonstrated that either shielding type SA or type SB can achieve good isolation between adjacent coil modules whether in the flat or bending condition. The peak values and the corresponding frequencies of S_{21} magnitude of the PEC dual-loop probe

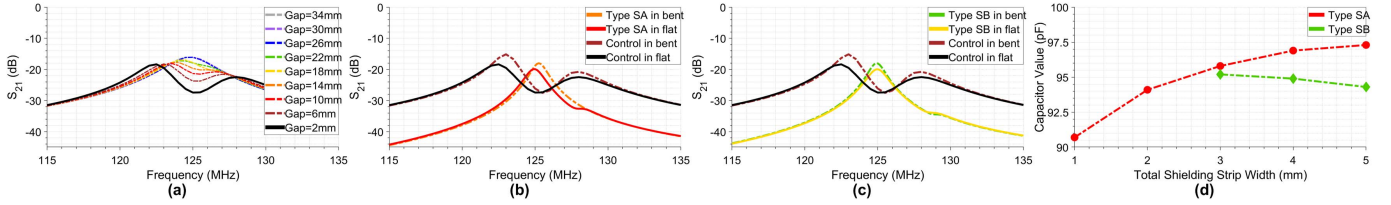


Fig. 3. (a) Numerical simulations of $|S_{21}|$ of the PEC dual-loop probe when two control coils were placed side-by-side with different gap distances. The control coils without help of shielding required a gap larger than 26 mm to achieve sufficient isolation between coils. (b) – (c) Numerical simulations of $|S_{21}|$ when a two-channel coil array equipped with shielding type SA or type SB in the flat (solid curves in red or yellow) or bending (dashed curves in orange or green) condition. These arrays achieved a sharp peak whether in the flat (solid curve in black) or bending (dashed curve in brown) condition without the need of adjusting capacitance value. The overlapping curves demonstrated small frequency drifts of less than 0.25 MHz for shielding type SA and 0.125 MHz for type SB. (d) Numerical simulations of tuning capacitance values with respect to the total shielding strip width. Notice that shielding type SA showed a positive and larger slope value, while type SB showed a negative and smaller one.

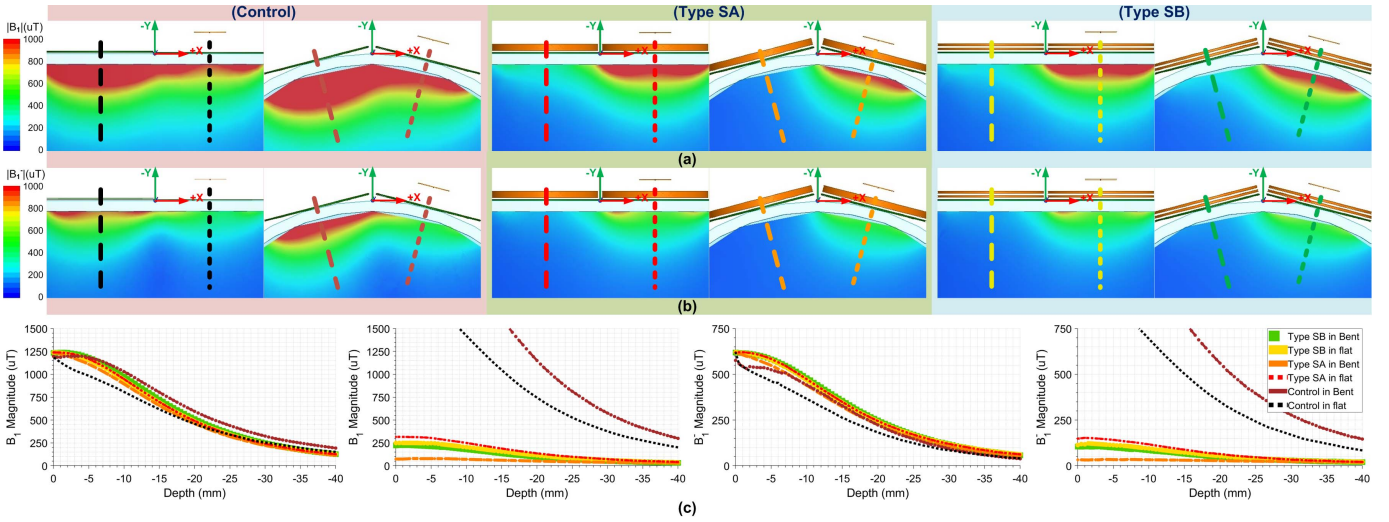


Fig. 4. Numerical simulations of normalized (a) $|B_1|$ and (b) $|B_1^-|$ maps on the central axial plane when a two-channel coil array without or with a shielding structure was in the flat or bending condition. Dotted and dashed lines in different colors indicate the profiles along the normal line through the center of circular coil in the positive and negative X-axes, respectively. (c) The corresponding profiles of normalized B_1 magnitude in the positive (left) and negative (middle left) X-axes, and normalized B_1^- magnitude in the positive (middle right) and negative (right) X-axes. Depth was measured from the phantom surface.

were summarized in Table I. The S_{21} magnitude maximum in the bending condition shifted less than 0.25 MHz from 125 MHz for shielding type SA and 0.125 MHz for type SB. Fig. 3(d) shows the relationship of tuning capacitance and the total shielding strip width. For shielding type SB, this total width was the sum of two strips and the interior gap width. The slope was $+6.6 \text{ pF}/4 \text{ mm}$ of shielding type SA and $-0.9 \text{ pF}/2 \text{ mm}$ of type SB. We found that larger tuning capacitance values were needed for wider shielding strip for shielding type SA. Nevertheless, the shielding type SB presented a negative correlation and a smaller deviation.

Fig. 4(a) and Fig. 4(b) shows the simulations of normalized B_1 and B_1^- magnitude maps on the central axial plane when a two-channel coil array equipped without or with shielding structure was placed on the flat surface or bent to fit the curved surface of a cylindrical phantom. Fig. 4(c) shows the magnitude profiles along the normal line perpendicular to the coil surface through the center of circular coils. Comparing to the two-channel control coil along the normal line through the center of circular coil in the negative X-axis, a two-channel coil array with either shielding type had the normalized B_1^-

magnitude of $14.4 \pm 1.7\%$ (at 5 mm depth from the coil surface) and $21.8 \pm 1.0\%$ (at 35 mm depth from the coil surface) in the flat condition, and $5.1 \pm 2.5\%$ (at 5 mm depth from the coil surface) and $11.3 \pm 0.7\%$ (at 35 mm depth from the coil surface) in the bending condition. These simulation results indicated that the two-channel coil arrays with either shielding type SA or type SB in different bending conditions induced a similar B_1^- magnitude. They also exhibited better isolation beneath the circular coil, compared to the case that the two-channel control coil showed strong magnetic flux coupling. Notice that shielding type SA showed a larger difference between the two profiles in the negative X-axis in the flat and bending conditions than that of type SB. Detailed field magnitude values and the calibrated excitation power in the numerical simulations were summarized in Table I. Notice that the control coil had a lower magnetic field strength in the positive X-axis, because of the obvious magnetic flux coupling to the coil in the negative X-axis. This led to a much large excitation power for the control coil in either flat or bending condition in order to achieve the desired flip angle at the center of coil in the positive X-axis.

TABLE I
RESULTS OF NUMERICAL SIMULATION OF THE TWO-CHANNEL COIL ARRAY

Shielding Type	Control	Type SA	Type SB
Peak S_{21} magnitude and the corresponding frequency	N/A (due to Split peaks)	Flat: -19.91 dB @125.0 MHz Bent: -18.02 dB @125.25 MHz	Flat: -19.94 dB @125.0 MHz Bent: -18.03 dB @ 124.875 MHz
Tuning capacitance value (pF)	57.8	95.8	95.2
Variance in tuning capacitance value (pF)	N/A	90.7 to 97.3	95.2 to 94.3
B_1^* magnitude at -5/-20/-35 mm along the normal line through the center of circular coil in the positive X-axis (μT)	Flat: 463/ 183/ 59 Bent: 525/ 223/ 60	Flat: 584/ 245/ 86 Bent: 548/ 224/ 75	Flat: 579/ 243/ 84 Bent: 582/ 248/ 82
B_1^* magnitude at -5/-20/-35 mm along the normal line through the center of circular coil in the negative X-axis (μT)	Flat: 889/ 350/ 121 Bent: 1311/ 561/ 199	Flat: 142/ 65/ 28 Bent: 34/ 28/ 21	Flat: 113/ 54/ 25 Bent: 100/ 48/ 24
Excitation power values after calibrating as Eq. (2) (Watt)	Flat: 8.06 Bent: 10.31	Flat: 1.20 Bent: 0.75	Flat: 1.20 Bent: 0.82

B. Imaging Measurements

All the coil modules equipped without or with shielding structure were manually tuned to the resonance frequency 123.25 MHz and matched to 50Ω . The S_{21} magnitudes of the custom-made dual-loop probe between two adjacent coils with shielding type SA or type SB were in the range of -29.6 dB and -28.3 dB under the loaded condition without attached to a preamplifier. Preamplifier decoupling reduced the S_{21} magnitudes of the custom-made dual-loop probe by about 31 dB. The S_{21} magnitude difference between tuned and detuned conditions was around 34 dB. The measured unloaded and loaded Q values for a single-channel control coil were about 117 and 55, respectively, for a single-channel coil with shielding type SA were about 77 and 54, respectively, and for a single-channel coil with shielding type SB were about 79 and 54, respectively.

Fig. 5 shows the experimental measurements of SNR profile along the normal line through the center of a single-channel coil equipped without or with shielding type SB when this coil was placed on or lifted up from the surface of acrylic hemispherical phantom. The results indicated that the advantage of SNR of a circular coil without any shielding structure diminished as the imaging object was placed about 8 mm or farther away from the coil.

Fig. 6 shows the experimental SNR maps on the axial plane through the center of hemispherical phantom when a two-channel coil array was placed on the flat surface or bent to fit the curved surface of hemispherical phantom. All coil modules conducted in the imaging experiments applied the preamplifier decoupling whether without or with shielding structure. We found that the control coils had coupling between each other, whereas the coil modules with either shielding type SA or type SB had better isolation. Notice that both arrays with shielding type SA and type SB showed this isolation whether the array was bent in a large or small angle between coil modules (Fig. 6(a) to Fig. 6(d)). This result suggested that the two-channel coil arrays with shielding type SA or type SB had better isolation between adjacent coil modules when the array

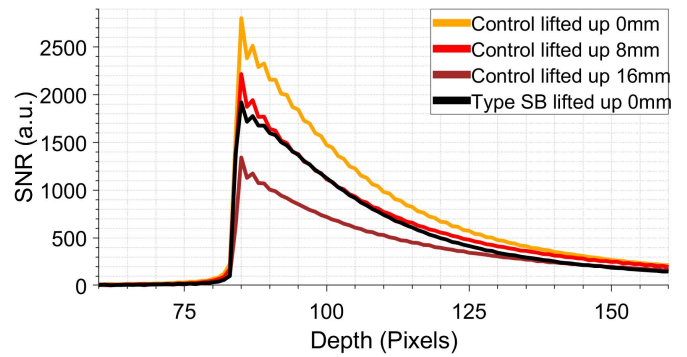


Fig. 5. Experimental SNR profiles along the normal line through the center of a single-channel coil equipped without or with shielding type SB. The advantage of image SNR of the control coil diminished when the distance from the imaging object was larger than about 8 mm. Depth was measured from the phantom surface in image pixel which was about 0.7 mm.

is bent differently at all degrees of curvature. The magnitudes of off-diagonal element in the 2×2 noise correlation matrix for the two-channel control coil, the two-channel coil array with shielding type SA, and the two-channel coil array with shielding type SB ranged between 0.28 and 0.44, 0.08 and 0.17, and 0.09 and 0.13, respectively. As all array applied the same technique of preamplifier decoupling, this difference was attributed to the difference of the stacked shielding structure. Fig. 6(e) shows the SNR profiles of the single-channel coil in the positive X-axis along the normal line perpendicular to the coil surface through the center of circular coils. Comparing to a two-channel coil array without a shielding structure, the two-channel coil array equipped with shielding type SA or type SB shows a lower SNR distribution in the negative X-axis. The maximum SNR of coil array with shielding type SA or type SB in the negative X-axis was reduced by between 24.7% and 26.6% or between 23.8% and 26.5%, respectively, in different bending conditions.

Fig. 7(a) and Fig. 7(b) show the experimental SNR maps on the axial plane through the center of a hemispherical phantom using either a commercial 32-channel head coil array or a

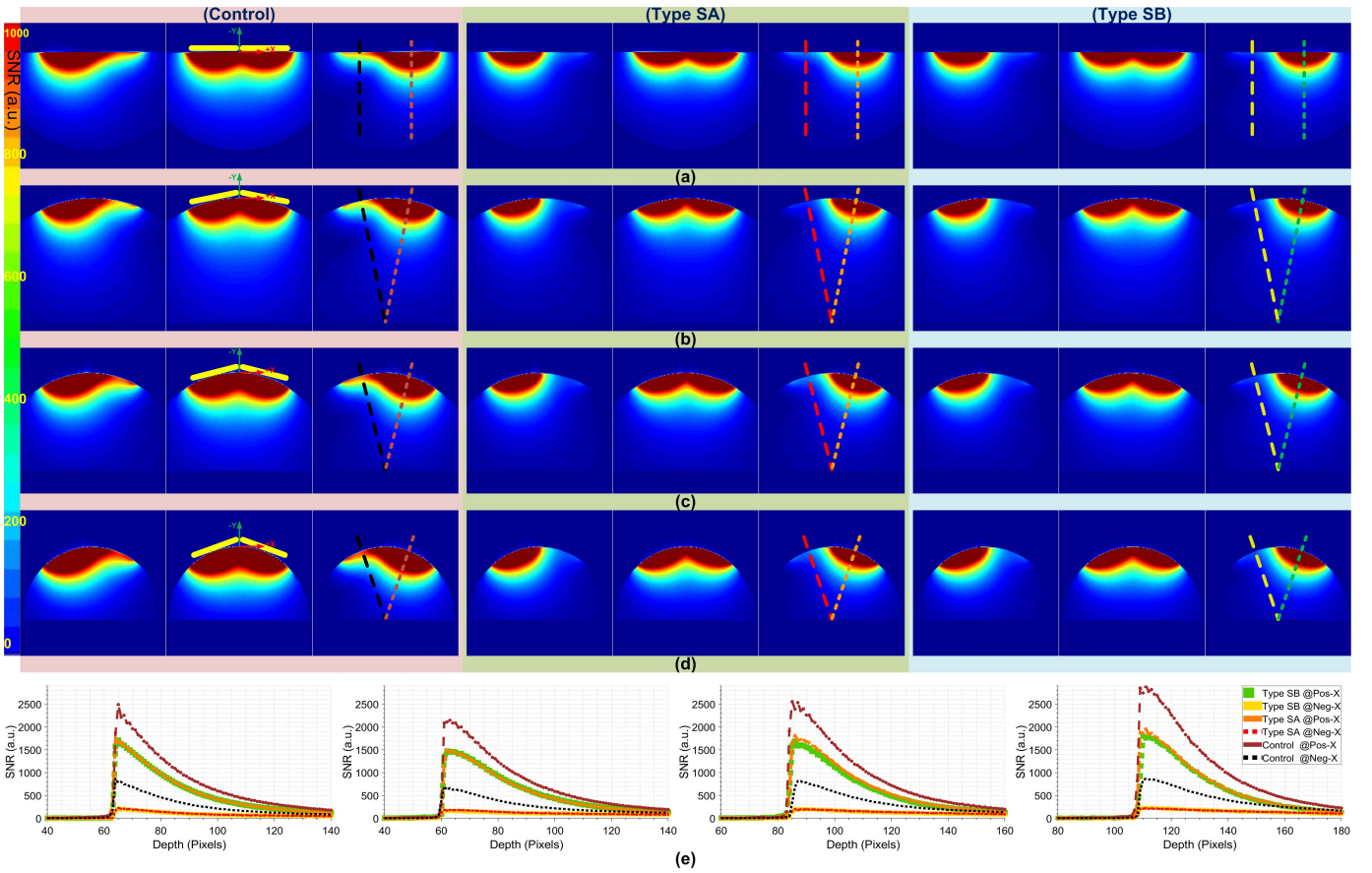


Fig. 6. Measurements of RSS SNR map when a two-channel coil array equipped without any shielding structure (the leftmost three columns), with shielding type SA (the central three columns), or with type SB (the rightmost three columns) was placed on (a) the flat surface of a hemispherical phantom, (b) the curved surface of a hemispherical phantom of 250 mm diameter, (c) the curved surface of a hemispherical phantom of 200 mm diameter, and (d) the curved surface of a hemispherical phantom of 150 mm diameter. (e) SNR profiles along dashed lines in (a), (b), (c), and (d) of the single-channel coil in the positive X-axis on a flat surface (left), a curved surface with radius of 250 mm (middle left), 200 mm (middle right), and 150 mm (right). The SNR curves of coils with shielding type SA and type SB were very much overlapped.

4-channel flexible coil array. Fig. 7(c) to Fig. 7(e) shows the experimental SNR maps using our seven-channel flexible coil array equipped with shielding type SB. Comparing to the 32-channel head coil array, our seven-channel flexible coil array had 3.2-fold gain in the maximum SNR while including the SNR advantage introduced by smaller-diameter coils within smaller depth. Notice that the flexible coil array in Fig. 7(e) was shifted from the curved surface (about 5° to 6° at right and 10° to 12° at left) to demonstrate the coil performance when it was not tightly fitted to the phantom surface. These bending between coils caused different SNR reduction at both sides. Fig. 7(f) to Fig. 7(j) show the corresponding noise correlation matrices. Our seven-channel flexible coil array did not show visible change in the coupling between coil modules whether the array was in the flat or bending condition. The maximum and average of off-diagonal entries of the noise correlation matrix of our seven-channel flexible coil array were similar or even lower than those of commercial coil arrays.

C. Human Imaging

Fig. 8(a) to Fig. 8(c) show the SNR maps using a commercial 32-channel head coil array, a 4-channel flexible coil array, and our seven-channel flexible coil array equipped with

shielding type SB for human head, calf, and knee imaging, respectively. Comparing SNR profiles to those of the 32-channel head coil array and the 4-channel flexible coil array along the yellow line through the center of axial images shown in Fig. 8(d) and Fig. 8(e), our seven-channel flexible coil array exhibited 2.63-fold/3.89-fold gain in maximum SNR and higher SNR at locations no deeper than 29.9/25.7 mm from the coil surface, respectively. They also had 1.35-/1.50-fold gain in the average SNR within the 50 mm depth from the surface. These SNR advantages may be related to a smaller coil diameter in our flexible coil array.

Fig. 8(g) shows the human brain images using our seven-channel flexible coil array equipped with shielding type SB placed around the right temporal lobe. Fig. 8(h) and Fig. 8(i) show the anatomical images acquired with the same coil array wrapped around the calf and the knee of the subject. Clear contrast between gray matter and white matter can be observed in the brain images. Tibia and fibula can be clearly seen in the calf and knee images using our seven-channel flexible coil array. Neither obvious artifact nor signal void due to coil gap was found in anatomical images of head, calf, and knee acquired with our coil with the matched size of stacked shielding structures.

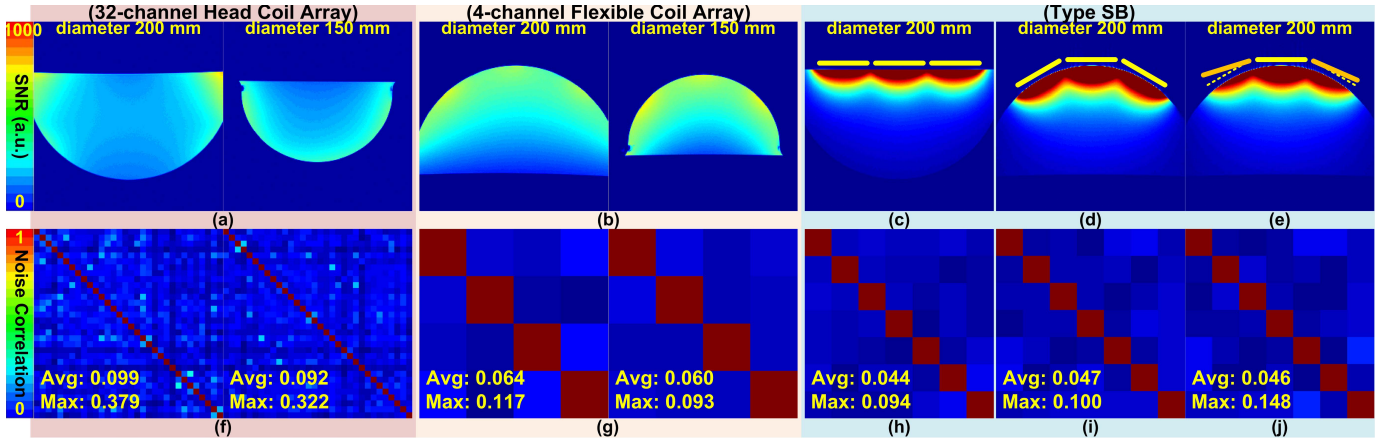


Fig. 7. Experimental measurements of RSS SNR map when a commercial (a) 32-channel head coil array, (b) 4-channel flexible coil array, or (c) – (e) our seven-channel flexible coil array equipped with shielding type SB was placed on the flat or curved surface of an acrylic hemispherical phantom. (e) shows the SNR map from the same seven-channel array with shielding type SB but incompletely fitted to the curved surface. Dashed lines in yellow and solid lines in orange indicate the different bending conditions. (f) – (j) show the noise correlation matrices of (a) – (e).

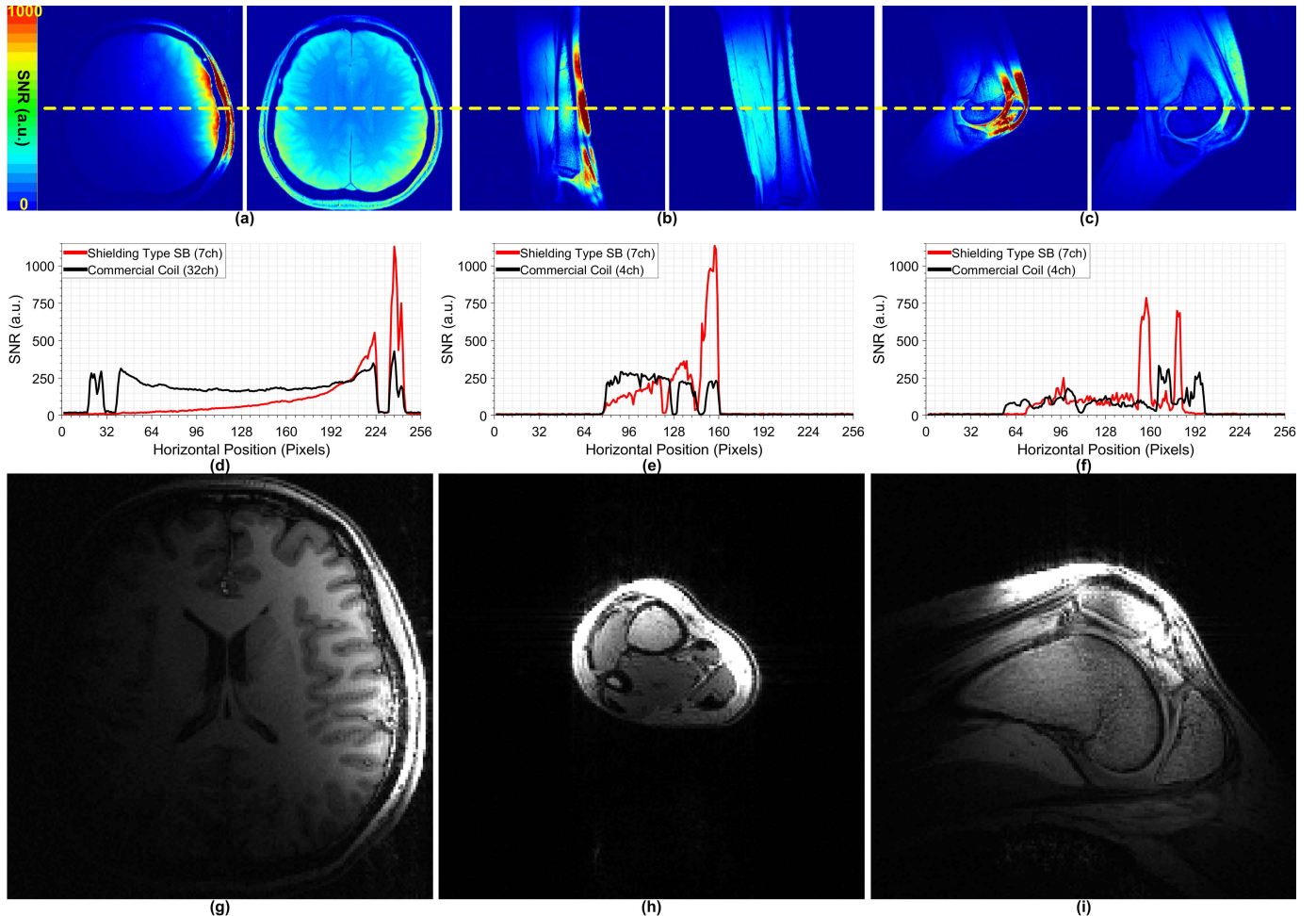


Fig. 8. (a) RSS SNR maps of the seven-channel flexible coil array equipped with shielding type SB (left) vs. the commercial 32-channel head coil array (right). The average SNR within 50 mm depth of the seven-channel flexible coil array was 35.4% higher than that of the commercial 32-channel head coil array. RSS SNR maps at calf (b) and knee (c) of the seven-channel flexible coil array with shielding type SB (left) vs. the commercial 4-channel flexible coil array (right). The average SNR gain within 50 mm depth of the seven-channel flexible coil array was 1.35-fold (calf) and 1.50-fold (knee), comparing to that of a commercial 4-channel flexible coil array. (d) – (f) The corresponding SNR profiles of (a) – (c). Representative anatomical images acquired using our seven-channel flexible coil array on the (g) brain, (h) calf, and (i) knee, respectively, of a participant.

IV. DISCUSSION

A flexible and modular coil array can be highly valuable when pursuing a universal-purpose receiver coil array suitable for different anatomical contours. Different from the

conventional techniques to decouple adjacent coils, we proposed two circumferential shielding structures stacked above the coil and utilized a 2-mm gap to achieve a flexible coil array with good decoupling. Comparing to a rigid coil array

that decouples between coils by overlapping, our flexible and modular coil array tolerated the image SNR loss due to the inevitable shielding of magnetic flux. Comparing to previous works, the unloaded Q values and unloaded-loaded Q ratios with a shielding structure were relatively low. This suggests that the dominant noise source in our work was conductor loss from the coil, shielding structure, and associated circuits. The optimal distance between dual-loop probe and coils equipped with a shielding structure to achieve critical coupling was around 10 mm, significantly different from that for control coils, which had the optimal distance of about 35 mm. This also suggests that the shielding structure caused more coil loss and lower unloaded Q values. As there was dominant noise caused by copper loss, shielding a coil reduced SNR. Despite the compromised SNRs, our flexible coil array can tightly fit to the imaging object and consequentially improve the filling factor and a higher sensitivity than a rigid coil array, which often suffers a SNR loss due to the gap between coils and between coils and the imaging object. Furthermore, the modular coil design provided the feasibility to create different coil arrays for imaging different human body parts.

It is well known that even a gap between adjacent coils can provide sufficient decoupling. But the gap needed is approximately half of the coil diameter (as indicated in Fig. 3(a)). Such a gap inevitably introduces a signal void between adjacent coil modules. Our proposed shielding structure, with either shielding type SA or type SB, can provide sufficient isolation with a small gap and keep the coil module in resonance without the need of adjusting capacitance values, even when the coil array was in different bending conditions. These results suggest that our proposed coil array can support a wide change of coupling loading. It is possible to get similar result of high isolation using a conventional shielding [19] because of geometric similarity. However, the gap between coils may be larger than our design. Actually, when a specific set of coil dimensions is demanded, the corresponding optimal shapes and sizes of circumferential shielding structure (whether stacked or coplanar) should be carefully evaluated in order to simultaneously obtain the minimal mutual coupling between coil modules and the maximal SNR.

Notice that the proposed module including the coil conductor and the coil substrate were kept rigid when fitting on surfaces with different curvature. However, this can restrict the degree of fitting to the imaging object. Therefore, we chose a medium size as the coil diameter to maximize the bending capability of the whole coil array. In this work, we defined 50 mm as the coil diameter to construct the proof-of-concept flexible coil array. This choice of diameter was beneficial to imaging small to medium anatomical targets with a significant curvature, such as adult limbs and pediatric heads. Such coils with a relatively small diameters also contributed to higher SNR. But the choice of a small diameter, we had a smaller FOV and lower SNR at locations away from the coil. Our next step is to build a new coil array with a mixture of coil modules of small, medium, and large diameters. We expect the new hybrid array will increase the flexibility for imaging for a wider range of anatomical targets.

The simulation results (Fig. 3(b) and Fig. 3(c)) showed that the shielding type SB exhibited higher consistency in different bending conditions with a smaller drift of peak frequency than that of the shielding type SA. The simulation results (Fig. 4) showed that the shielding type SA exhibited slightly higher B_1^- magnitude but less consistent B_1^- in different bending conditions, whereas shielding type SB provided similar isolation. The simulation results (Fig. 3(d)) showed a positive and larger slope of the relationship between the tuning capacitance and the shielding strip width for shielding type SA, whereas a negative and smaller slope of the relationship for shielding type SB. These observations were consistent with the knowledge that the circumferential shielding type SA (a single strip with different strip widths) behaves as a “magnetic-wall” that traps the magnetic flux and causes a field concentration effect. Such a “wall” may induce a smaller effective coil inductance. The larger slope is equivalent to higher sensitivity in change of inductance and loading. In contrast, our circumferential shielding type SB (two parallel strips with a gap between) can compensate the shortcoming of shielding type SA by keeping the tuning capacitance in a reasonable range. In addition, the smaller variation of capacitance of the shielding type SB suggested an obvious advantage that the manufacture error in shielding strip width may cause less performance variation. In the near future, a more complex combination of shielding type SA and type SB (e.g. multiple shielding strips with tiny widths) will be studied to integrate their different advantages.

Our experimental results agreed with the simulation results that both shielding type SA or type SB achieved high isolation between neighboring coil modules, even when the coil array was bent to fit the surfaces of different curvatures. The root-mean-square (rms) values of B_1^+ and the average RF powers were experimentally measured on the same phantom using a gradient-echo pulse sequence for several cases: a single-channel coil equipped without or with the stacked shielding structure, a two-channel coil array without or with shielding structure among that one coil kept detuning. The rms values of B_1^+ and average RF powers were reported by the scanner. We found that the rms values of B_1^+ and average RF powers were in the range between 0.5 to 0.6 μT and 1.5 to 1.6 Watt, respectively, across all experiments. The shielding structure of a detuned coil did not generate any artifact on the image of the other coil of two-channel coil array. These results suggested that stacked shielding structures did not introduce artifacts to deteriorate the transmit field homogeneity. The shielding structure did not significantly change the flip angle to cause safety concern, either.

Despite the possible changes in relative positions between coil modules and changes in mutual inductance and capacitive coupling between coils and the object, our coil array with either shielding structures had similar SNR distributions and low off-diagonal entries of noise correlation matrices without the need of adjusting capacitance values. These results suggested that the image quality was similar in different bending conditions. We compared the commercial coil arrays with our flexible coil array (Fig. 7 and Fig. 8). Our seven-channel

flexible coil array exhibited as high as 3.89-fold gain in maximum SNR, relatively higher SNR advantage within 50 mm depth from the superficial layer. However, we were aware that the distinct noise volume of each coil could cancel out a certain degree of our SNR advantage in these comparisons. Although the dimensional differences between coils definitely introduced certain deviation into the result comparisons, our experimental results in Fig. 5 and Fig. 7(e) demonstrated the SNR benefit of a flexible coil array cable of tightly fitting to the surface of imaging objects. While we only demonstrated this coil array prototype for MR imaging of human brain and extremity, the same design is applicable to fit other human body parts.

V. CONCLUSION

This work demonstrates a flexible and modular coil array to image different human anatomical targets. The advantage of the proposed coil shielding structures is removing the restriction on overlapping between coil modules in order to achieve sufficient decoupling. We utilized two types of stacked circumferential shielding structures together with a surface coil to implement the modular coil array. We constructed a coil array suggested by numerical simulations and performed imaging experiments to demonstrate that the coil array with the proposed shielding structures can conform to the contour of the imaging object and achieve good isolation with high image SNR for versatile anatomical targets, including human brain, calf, and knee. In the future, we will construct multi-purpose coil arrays with a mixture of coil modules of different sizes, shielding geometries, and a flexible housing designed for *in vivo* imaging with different clinical requirements.

REFERENCES

- [1] P. B. Roemer, W. A. Edelstein, C. E. Hayes, S. P. Souza, and O. M. Mueller, "The NMR phased array," *Magn. Reson. Med.*, vol. 16, no. 2, pp. 192–225, 1990.
- [2] D. K. Sodickson and W. J. Manning, "Simultaneous acquisition of spatial harmonics (SMASH): Fast imaging with radiofrequency coil arrays," *Magn. Reson. Med.*, vol. 38, no. 4, pp. 591–603, 1997.
- [3] K. P. Pruessmann, M. Weiger, M. B. Scheidegger, and P. Boesiger, "SENSE: Sensitivity encoding for fast MRI," *Magn. Reson. Med.*, vol. 42, no. 5, pp. 952–962, 1999.
- [4] J. A. de Zwart, P. J. Ledden, P. Kellman, P. van Gelderen, and J. H. Duyn, "Design of a SENSE-optimized high-sensitivity MRI receive coil for brain imaging," *Magn. Reson. Med.*, vol. 47, no. 6, pp. 1218–1227, 2002.
- [5] B. Keil *et al.*, "Size-optimized 32-channel brain arrays for 3 T pediatric imaging," *Magn. Reson. Med.*, vol. 66, no. 6, pp. 1777–1787, 2011.
- [6] J. A. Nordmeyer-Massner, N. De Zanche, and K. P. Pruessmann, "Stretchable coil arrays: Application to knee imaging under varying flexion angles," *Magn. Reson. Med.*, vol. 67, no. 3, pp. 872–879, 2012.
- [7] R. Kriegel *et al.*, "Novel inductive decoupling technique for flexible transceiver arrays of monolithic transmission line resonators," *Magn. Reson. Med.*, vol. 73, no. 4, pp. 1669–1681, 2015.
- [8] I. Hancu, E. Fiveland, K. Park, R. O. Giaquinto, K. Rohling, and F. Wiesinger, "Flexible, 31-channel breast coil for enhanced parallel imaging performance at 3 T," *Magn. Reson. Med.*, vol. 75, no. 2, pp. 897–905, 2016.
- [9] J. R. Corea *et al.*, "Screen-printed flexible MRI receive coils," *Nature Commun.*, vol. 7, p. 10839, Mar. 2016.
- [10] J.-N. T. Yeh and F. H. Lin, "Decoupling between coils in a flexible phased-array using stacked circumferential shielding," in *Proc. 24th Annu. Meeting (ISMRM)*, Singapore, 2016, p. 3522.
- [11] J.-N. T. Yeh and F. H. Lin, "Magnetic resonance imaging receiver coil decoupling using circumferential shielding structures," in *Proc. IEEE Eng. Med. Biol. Soc.*, Orlando, FL, USA, Aug. 2016, pp. 6254–6257.
- [12] S. S. Vasanawala *et al.*, "Development and clinical implementation of very light weight and highly flexible AIR Technology arrays," in *Proc. 25th Annu. Meeting (ISMRM)*, Honolulu, HI, USA, 2017, p. 755.
- [13] R. F. Lee, R. O. Giaquinto, and C. J. Hardy, "Coupling and decoupling theory and its application to the MRI phased array," *Magn. Reson. Med.*, vol. 48, no. 1, pp. 203–213, Jul. 2002.
- [14] B. Wu *et al.*, "7 T human spine imaging arrays with adjustable inductive decoupling," *IEEE Trans. Biomed. Eng.*, vol. 57, no. 2, pp. 397–403, Jun. 2010.
- [15] A.-L. Perrier *et al.*, "Design of a two-channel NMR coil using an impedance transformation approach," *IEEE Sensors J.*, vol. 12, no. 6, pp. 1801–1808, Jun. 2012.
- [16] X. Yan, X. Zhang, B. Feng, C. Ma, L. Wei, and R. Xue, "7 T transmit/receive arrays using ICE decoupling for human head MR imaging," *IEEE Trans. Med. Imag.*, vol. 33, no. 9, pp. 1781–1787, Sep. 2014.
- [17] M. Weiger, K. P. Pruessmann, C. Leussler, P. Röschmann, and P. Boesiger, "Specific coil design for SENSE: A six-element cardiac array," *Magn. Reson. Med.*, vol. 45, no. 3, pp. 495–504, Mar. 2001.
- [18] B. Keil and L. L. Wald, "Massively parallel MRI detector arrays," *J. Magn. Reson.*, vol. 229, pp. 75–89, Apr. 2013.
- [19] T. Lanz and M. Griswold, "Concentrically shielded surface coils—A new method for decoupling phased array elements," in *Proc. 14th Annu. Meeting (ISMRM)*, Seattle, WA, USA, 2006, p. 217.
- [20] M. Burl and I. Young, "Surface receiver coils with asymmetric sensitivity on either side for MR imaging and spectroscopy," in *Proc. 2nd Annu. Meeting (ISMRM)*, New York, NY, USA, 1994, p. 1128.
- [21] N. De Zanche, J. A. Massner, C. Leussler, and K. P. Pruessmann, "Modular design of receiver coil arrays," *NMR Biomed.*, vol. 21, no. 6, pp. 644–654, 2008.
- [22] M. H. Deppe, J. Parra-Robles, H. Marshall, T. Lanz, and J. M. Wild, "A flexible 32-channel receive array combined with a homogeneous transmit coil for human lung imaging with hyperpolarized ^3He at 1.5 T," *Magn. Reson. Med.*, vol. 66, no. 6, pp. 1788–1797, 2011.
- [23] K. M. Gilbert, J. Belliveau, A. T. Curtis, J. S. Gati, L. M. Klassen, and R. S. Menon, "A conformal transceive array for 7 T neuroimaging," *Magn. Reson. Med.*, vol. 67, no. 5, pp. 1487–1496, 2012.
- [24] B. Wu *et al.*, "Flexible transceiver array for ultrahigh field human MR imaging," *Magn. Reson. Med.*, vol. 68, no. 4, pp. 1332–1338, Jan. 2012.
- [25] A. Graessl *et al.*, "Modular 32-channel transceiver coil array for cardiac MRI at 7.0 T," *Magn. Reson. Med.*, vol. 72, no. 1, pp. 276–290, 2014.
- [26] J. Cui *et al.*, "A switched-mode breast coil for 7 T MRI using forced-current excitation," *IEEE Trans. Biomed. Eng.*, vol. 62, no. 7, pp. 1777–1783, Jul. 2015.
- [27] T. Zhang *et al.*, "A semiflexible 64-channel receive-only phased array for pediatric body MRI at 3 T," *Magn. Reson. Med.*, vol. 76, no. 3, pp. 1015–1021, 2016.
- [28] X. Yan, J. C. Gore, and W. A. Grissom, "Self-decoupled RF coils," in *Proc. 25th Annu. Meeting (ISMRM)*, Honolulu, HI, USA, 2017, p. 757.
- [29] D. I. Hoult, "The principle of reciprocity in signal strength calculations—A mathematical guide," *Concepts Magn. Reson.*, vol. 12, no. 4, pp. 173–187, 2000.
- [30] C. M. Collins and M. B. Smith, "Calculations of B_1 distribution, SNR, and SAR for a surface coil adjacent to an anatomically-accurate human body model," *Magn. Reson. Med.*, vol. 45, no. 4, pp. 692–699, 2001.